Algorithms to improve spectral discrimination from Indian hyperspectral sensors data

A. Senthil Kumar[1],*, V. Keerthi[1], V. K. Dadhwal[1] and A. S. Kiran Kumar[2]

[1]Geophysical and Special Products Group, National Remote Sensing Centre (ISRO), Balanagar, Hyderabad 500 037, India
[2]Space Applications Centre (ISRO), Jodhpur Tekra, Ahmedabad 380 015, India

With the inclusion of a hyperspectral imager (HySI) sensor on the Indian Mini Satellite (IMS-1) Earth observation mission and subsequently near identical hyperspectral sensor on the Chandrayaan-1 lunar mission, 64-band hyperspectral data from both these missions have provided the user community rich information to explore new algorithms to exploit sensor-specific parameters and to interpret and/or classify the features in multi-resolution frame. In this article, methods to improve spectral uniqueness present in the HySI by analysing adjacent bands' spectral overlaps, by implementing spectral deconvolution and reconstruction techniques are presented. Similarly, the use of multi-resolution approach for fast searching of standard spectral library end-members for better discrimination of hyperspectral pixel data are also discussed along with applications in Earth and lunar surface hyperspectral image interpretation. These spectral analyses techniques are useful in discriminating subtle differences in spectral signatures that help study the origin of secondary craters and gullies/ landslides on the lunar surface.

Keywords: Lunar surface, multi-resolution approach, spectral deconvolution, spectral overlap.

Introduction

SPECTRAL signatures inferred from numerous contiguous spectral channels in the visible-to-near infrared (VNIR) regions of the electromagnetic spectrum typical of hyperspectral imaging sensors are capable of providing subtle spectral variations in surface materials, which in turn help to discriminate these from one another. Exploration of new techniques and algorithms for processing of hyperspectral images (HySI) is useful in application areas that include surface mineralogy, military surveillance, water quality, soil type and erosion, vegetation type, plant stress, leaf water content and canopy chemistry, crop type and condition as well as planetary surface evolution.

From image-processing point of view, the HySI pixel can be viewed as a column vector (also known as hypercube) formed by pixels of each band to form spatial–spectral dimensions. Finding appropriate tools and approaches for visualizing and analysing the essential information in a hyperspectral scene remains an area of active research.

The HySI in material classification is compounded with a coarse-ground pixel size of the sensor for want of adequate sensor signal-to-noise ratio (SNR) as the signal strength through a fine spectral passband (defined as spectral response function (SRF) with bandwidth ~10–15 nm). To achieve narrow contiguous spectral profiles, the HySI sensor is typically designed to have overlapping bandwidths of the spectral bands to maximize the input light energy in each band range in order to ensure the required SNR. Swayze et al.[1] have shown that spectral bandwidth (BW) and sampling interval (SI) significantly influence the spectral identification of the surface materials. Here, BW refers to full-width at half maximum (FWHM) of the SRF of the hyperspectral sensor, and SI is the spectral distance between the centres of the adjacent bands. The BP and SI combination determines the spectral resolution which in turn dictates the material discrimination with instrument spectra in question. The hyperspectral instrument is said to be at Nyquist sampling (NS) when the ratio BP/(2·SI) is 1, or at critical sampling (CS) when (BP/SI) is 1. Under other conditions such as BP > 2 SI or BP < SI, the HySI is said to be either spectrally oversampled or under sampled respectively. When oversampling occurs, spectral details of the ground signal would get convolved with neighbouring channels, thus making bands less unique in spectral information content. On the other hand, under sampling is primarily limited by the detector array design, especially when there are gaps between adjacent detector elements, thus letting available light on the detector plane go unutilized. In most cases, the hyperspectral bands are, by design, oversampled.

This leads to development of sensor-specific correction algorithms using SRFs to obtain genuine spectral signature of a surface feature. The proposed approach, namely spectral deconvolution tries to artificially reduce effective bandwidth of each band, thereby attempting to resolve individual band spectrum as discrete as possible[2]. Kumar et al.[3] have recently shown that the spectral deconvolution could be effectively used to reduce the band overlap in the Indian Mini Satellite (IMS-1) HySI sensor

data, and have further suggested to limit to non-overlapping 17 bands from overlapped 64 bands. The description of method is further elaborated in the next section.

Similar to spectroscopic techniques in laboratory practice, surface material absorption features from spaceborne HySI data can be matched using a set of derived values, including depth and width at half-depth, or using the complete shape of the feature. Clark et al.[4] developed an expert system to organize these procedures at the USGS Spectroscopy Lab. Since the HySI bands are highly likely correlated, rational feature selection from the varieties of channels is important for effective analysis and information extraction of hyperspectral data for recognizing objects effectively and accurately[5]. Dealing with HySI, a huge number of channels generate high data redundancy[6]. The HySI data processing is best attempted from a high dimensional signal processing paradigm by virtue of its spectral bands into hundreds[7,8]. This is often referred to as the 'curse of dimensionality', and many new schemes have been proposed in recent years to tackle this for applications in classification[9–11]. Another limiting factor of the HySI data analysis is its moderately poor spatial resolution – again for want of the sensor SNR. This invariably makes multiple ground features jointly occupying into a single pixel, leading to spectrally mixed pixels. The interpretation of the mixed pixels is a key factor in the analysis of hyperspectral images[12].

Spectral mixture analysis involves the separation of a pixel spectrum into its end-member spectra and estimates the abundance value of each end-member in the pixel. Methods that exist till date can be classified into either linear or nonlinear[13]. Many of these approaches are based on spectral transformation of the hyperspectral image into its respective new domains. Besides the fact that these are computationally intensive, intermediate monitoring is not permissible, which may hinder expert's intervention in order to follow the performance and adapt any new approaches to meet the final objectives. Kumar et al.[14] proposed a multi-resolution analysis-based method, a fast search scheme known as variable interval spectral average (VISA). This method estimates local signature variations at multi-resolution scales to classify hyperspectral pixel from a set of centre wavelength peaks and their line profiles at each resolution. They further proposed a hybrid algorithm by combining VISA and spectral curve matching[15] to take advantage of both the methods to achieve higher classification accuracy[16]. The application of this method was first tested on a simulated image, and then on Chandrayaan-1 (referred to Ch-1 henceforth) HySI to analyse the geo-morphological features of the lunar surface[17].

Many impact craters are present on the lunar surface[18]. To understand the evolution process of planetary surfaces, it is important to study the geological activities of the primary craters and ejecta blankets around the pri-mary crater[19–21]. The origin and the spectral characteristics of secondary craters were analysed using Ch-1 Terrain Mapping Camera (TMC) and HySI. The findings have provided evidence for the secondary crater formation from low-velocity impact of clustered fragments[17,22]. We discuss these aspects in more detail later in the text. Gullies and landslides are observed on the interior wall of a crater in the Schrödinger basin on the far side of the moon. The spectral profiles from HySI, Moon Mineralogical Mapper (M3) images and morphological structures from high spatial resolution TMC images suggest that gullies and landslides are characterized by youthful dry granular flows[23,24]. This is further elaborated later in the text.

Sharpening HySI bands by spectral deconvolution

HySI was ISRO's first spaceborne hyperspectral sensor on-board IMS-1 launched on 28 April 2004 with spatial resolution of 505 m and spectral resolution of about 15 nm to cover the swath of 128 km for mapping the surface in 64 spectral bands in the visible and near infrared region (0.4–0.95 μm)[25]. This sensor was intended as an experimental payload to assess the performance prior to the one flown in Ch-1, the first Indian lunar mission[26]. The HySI sensor was one among the five Indian payloads that were flown in the Ch-1 mission launched in October 2008. The HySI instrument collected the reflected light from the lunar surface through a telecentric refractive optics and focused onto active pixel sensor area detector. The size of the area detector was 512×512 pixels. Spectral dispersion was done using varying coating thickness of wedge filter. The hyperspectral imager would actually acquire the data in 512 spectral bands in scan line direction, which would then be binned (integrated) by eight scan lines to realize the 64 spectral bands, and hence the signal was amplified by nearly 2.8 times (square root of 8). The output was 12-bit quantized data. The SNR of the HySI was greater than 100.

The individual channels of the HySI sensor, by design, are allowed to convolve or overlap with adjacent channels in order to achieve a continuous coverage of the spectrum. To extract the unique spectral content of these channels, however, it is necessary to apply techniques that may help band sharpening or reduction through the spectral deconvolution technique[2]. It is also preferred to recombine the resultant deconvolved channels to obtain a highly resolved spectrum. It has been shown that spectral overlapping has been reduced considerably to preserve the near-true spectra that can be achieved with the IMS-1 HySI data[3]. The overlapped region of the SRF can be compensated first by estimating the weighting factors of each neighbouring band and subtracting the weighted

neighbours from the original spectral data as given by in the equation[2]

$$L_{k,\text{dec}} = (L_{c,k} - L_{c,k+1}W_{k+a} - L_{c,k-1}W_{k-1})$$

$$\times \{R_k / (R_k - W_{k-1} - W_{k+1})\}, \qquad (1)$$

where $L_{k,\text{dec}}$ is the deconvolved spectral radiance of the kth spectral band, $L_{c,k}$ the convolved radiance of the kth band, $L_{c,k-1}$ and $L_{c,k+1}$ are the convolved radiance values of neighbouring bands, W_{k+1} and W_{k-1} are weights for neighbouring bands and R_k is the integral response given by integration of SRF, i.e. $\int R_k = S_k(\lambda)\mathrm{d}\lambda$. The weighting factors between two adjacent channels are computed from the overlapping spectral bands as

$$W_{k+1} = \sum \min(S_k, S_{k+1}) / \sum S_k.$$

After the channel data are deconvolved, these are again recombined to form high-resolution spectral data. The individual overlapping channels are combined to a highly resolved spectrum by linear superposition of these channel radiances multiplied with their weight factors as

$$L_{k,\text{recon}} = L_{k,\text{dec}} + L_{k+1,\text{dec}}W_{k+1} + L_{k-1,\text{dec}}W_{k-1}, \qquad (2)$$

where $L_{k,\text{recon}}$ is the reconstructed spectra, and W_{k+1} and W_{k-1} are the weighting factors corresponding to the nearest adjacent channels.

After applying the spectral deconvolution method, 20% overlap between neighbouring bands was reduced to 5% as shown in Figure 1, and required bands were further brought down to 17 non-overlapping bands. Spectral deconvolution and reconstruction algorithms described in
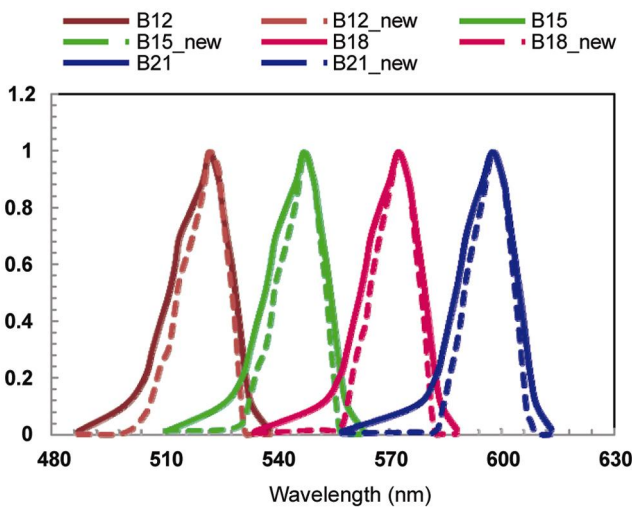
eqs (1) and (2) were applied to HySI. Some noise in the top of atmospheric (TOA) reflectance of ground targets was observed. This may be due to various factors, viz. sensor view angle, atmospheric noise, spectral deconvolution errors, etc. affecting the estimated TOA reflectance. To minimize this, spectral normalization was carried out. The spectral profile of the soil was chosen as reference, since no significant variation is present in the entire sensor spectral range. Spectral matching techniques such as spectral angle mapper (SAM) and spectral curve matching (SCM) were estimated between reference and image spectrum. The spectral curve for the vegetation is shown in Figure 2.

Hyperspectral data analysis using VISA technique

The VISA method, basically used to compute significant variations, if any, present in the signal by estimating 'local' or 'short-interval' variances. The short-interval variance is defined by

$$\tilde{f}(\lambda) = \hat{f}^2(\lambda) - [\hat{f}(\lambda)]^2. \qquad (3)$$

Here $\hat{f}(\lambda)$ is the average energy of the spectrum within the interval Δ, estimated from integral

$$\hat{f}(\lambda) = \frac{1}{\Delta} \int_{\lambda-\Delta/2}^{\lambda+\Delta/2} f(x)\mathrm{d}x \quad \text{window: } \Delta > 0. \qquad (4)$$

Application of the above equation results in a number of local maxima, say, M. The significant maxima are treated as signatures by setting a threshold θ to suppress unwanted background from entering into analysis. The VISA output can be written as

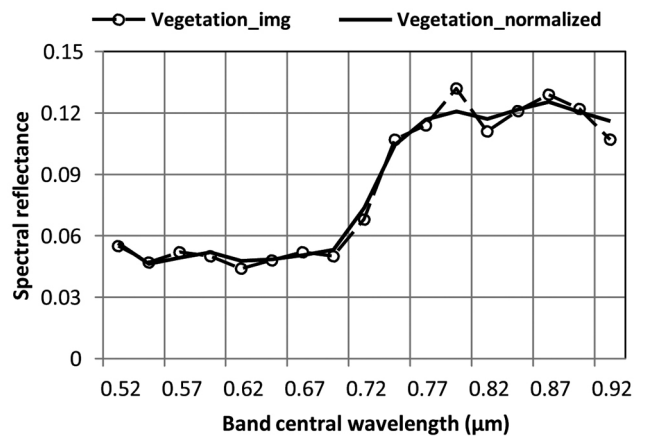$$D_{\text{visa}}(\theta) = \{\tau \in M : \hat{f}(\tau) \geq \theta\}. \qquad (5)$$

Figure 1. Effect of spectral deconvolution in reducing the effective bandwidth. The bold lines show the original SRFs of the bands, while the dotted lines show results after deconvolution. The overlap between adjacent bands can be seen to have reduced from nearly 20% to 5% after SD[3].

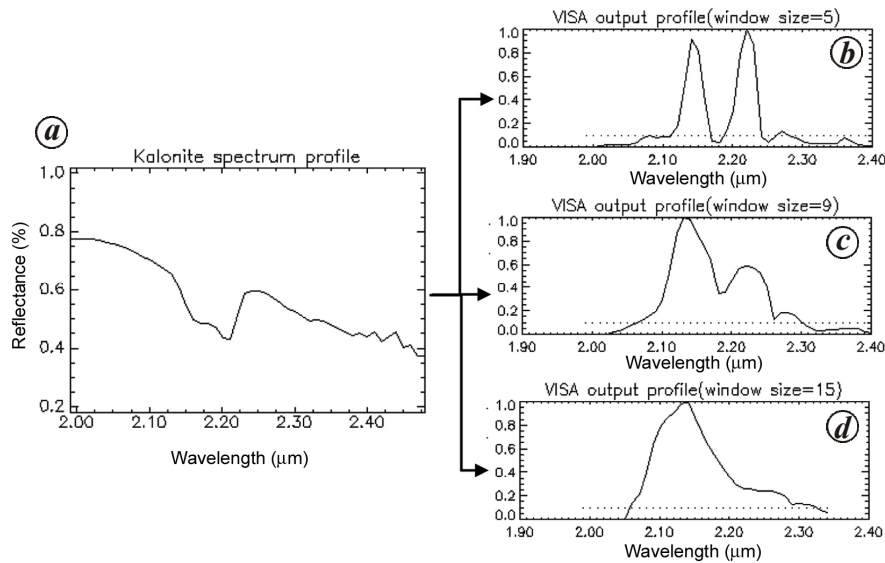**Figure 2.** Effect of normalization on image-derived spectral profile.

Figure 3. Multi-resolution analysis of the hyperspectral curve. *a*, A sample spectral profile of the kaolinite mineral. *b–d*, The normalized VISA output plots for spectral window sizes of (*b*) 5 (= 0.05 μm), (*c*) 9 (= 0.09 μm) and (*d*) 15 (= 0.15 μm).

The VISA scheme is thus capable of detecting both the local variations of the signal as well as the broad background variation in a way much similar to multi-resolution analysis by wavelets[27]. Since there is no sub-sampling of the signal at different scales involved in VISA, it is easier to relate the features at different compared to wavelet-based methods. For spectral analysis, we need to compare the image spectra at a pixel with that of targetted materials spectra. We can use short spectral covariance of two functions, defined as

$$V_{fg}(\lambda) = \hat{fg}(\lambda) - \hat{f}(\lambda)\hat{g}(\lambda). \qquad (6)$$

The peak detection in this case is from a bivariate set by a simple extension of the univariate approach. Appropriate threshold (θ) is to be estimated; it was found sufficient to estimate the background signal outside the absorption band for the hyperspectral data. Figure 3 shows the example of hyperspectral curve decomposition into three different resolutions using the VISA method.

Parameters to distinguish are sum square difference of peak and/or sum square difference of FWHM to be the least between any two spectra and the pixel is assigned to a class label independently for which each of these values is at its minimum. The pixel is declared as 'unclassified', thus giving both these parameters equal bias in judging the final decision[6]. The shape of the spectrum for a mixed pixel of two materials will vary when the mixing proportions change. The mixed class is best considered as a separate class from homogeneous classes[15]. The results are promising, especially when applied to a simulated dataset of different minerals with selected regions of interest (roi) as shown in Figure 4. Classification accuracies are shown in Figure 5. As can be seen, the hybrid method shows higher classification accuracies for mixed classes while retaining similar accuracies for the primary or homogeneous classes. The average percentage accuracies are estimated to be 77.17, 66.42 and 94.46 respectively, for the proposed VISA, SCM and the hybrid methods.

Spectral methods for lunar morphological analysis

As mentioned earlier, the use of hyperspectral imager data of Ch-1 mission for spectral characterization of some geological features has been significant. Detailed discussion is beyond the scope of this article; for details, the reader is referred to Kumar et al.[17,24].

Spectral characterization of secondary craters

Secondary craters are largely smaller in size, and hence this study demands image data with high spatial, spectral and radiometric resolution. The study area is located in the mare region and approximately 475 km northeast of Copernicus crater and 100 km southeast of timocharis crater. The study area depicts a dense cluster of impact craters, consisting of two populations: fresh craters and buried craters. The fresh craters are bright with sharp rim and crater interiors, while the buried craters are shallow, degraded and have diffuse boundaries. To understand whether the secondary craters in the study area were formed by the impact of the Copernicus rays or from the more closer Timocharis ejecta, the Ch-1 HySI was used. Spectral signatures of all the relevant features were normalized to the Apollo 16 soil albedo measured in the

laboratory[28] before subjecting to the SAM, SCM and VISA spectral matching methods.

The NIR range (720–950 nm) was selected for further analysis due to high correlation in the visible range band data. The spectral angles between the study area (average of the four central mounds) and the Copernicus distal ray, Timocharis distal ejecta and mare, in the 720–950 nm spectral window are 3.32°, 4.36° and 5.05° respectively. The smallest angle indicates the strongest spectral similarity between the spectra of the sample and the Copernicus ray. Similar results obtained from the spectral correlation and VISA confirm the origin of the secondary craters primarily from the Copernicus rays[17].

Another approach to assign the observed surface features is to compare their optimal maturity or time at which they were likely to have been formed. Space weathering processes on the Moon such as micrometeorite bombardment and solar-wind ion bombardment affect the optical properties of an exposed lunar soil. Fisher and Pieters[29] developed an approach to determine the maturity of lunar soil from Clementine spectral data. This method is

Figure 4. Synthesized hyperspectral image with 19 spectral channels in spectral range 2.0–2.325 μm and different regions chosen for primary and mixed samples spectra[15].

Figure 5. Classification accuracy for the VISA, SCM and hybrid methods.

based on the relationship between the values of 750 nm/950 nm of reflectance of lunar soils and their measured Is/FeO values. The optical maturity (OMAT) index provides significant insights into composition and presence of immature debris at the above sites. OMAT values are calculated using the HySI reflectance spectra, following Lucey *et al.*[30] as given in eq. (7), and compared with the corresponding values from the Clementine UV–Vis data.

$$\text{OMAT} = \sqrt{[(\rho_{40} + 0.03)^2 + x(\rho_{63}/\rho_{40}) - 1.16)^2}. \qquad (7)$$

The OMAT values of the Ch-1 HySI data were found to be 0.3475, 0.3771, 0.1596 and 0.1581 respectively, for the study area, Copernicus ray, mare and the Thimocharis ray. These observations are consistent with a genetic relationship between the study area and the Copernicus rays[17].

Spectral interpretation of lunar gullies and landslides

Landslide and gully formation on the interior wall of a 7 km diameter simple crater emplaced in the Schrödinger basin centred at 75°S and 135°E and located ~450 km from the South Pole on the farside of the Moon were recently observed by Kumar *et al.*[24]. These features occur on the steep upper crater wall, where the slope is ~35°. The gullies show a typical alcove-channel-fan morphology similar to Martian gullies, but with less conspicuous channels. The Ch-1 HySI data help characterize the spectral properties of the gullies and landslides in the interior wall of the crater. The spectral profiles are compared with the outside crater ejecta (OCE) blanket of the host crater. The spectral matching methods such as spectral correlation similarity, SAM and VISA were employed for spectral association of these features with surface materials of other permanent features (ridges and floor).

When the spectra of the wall and floor materials are compared, the HySI spectra of the floor, ridge and floor materials show considerable similarity with that of the crater wall. Even though these materials are covered by the shadow, spectral profiles are still significant due to high radiometric sensitivity of the HySI sensor. The OMAT values were also calculated using the HySI reflectance spectra as given in eq. (7). The analysis showed that the OMAT values of the gullies and landslides (0.34–0.51) were much higher than those of the ejecta blanket (0.14), indicating that the gullies and landslides were characterized by youthful debris flows that were composed of sediments with high optical immaturity.

Conclusions

Spectral deconvolution and reconstruction techniques are shown to be useful to obtain the genuine spectral signatures from the hyperspectral imaging sensor of the ground target, which was considerably overlapped with neighbour-
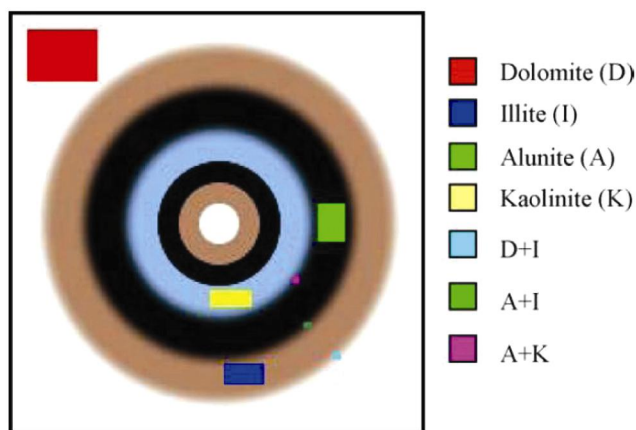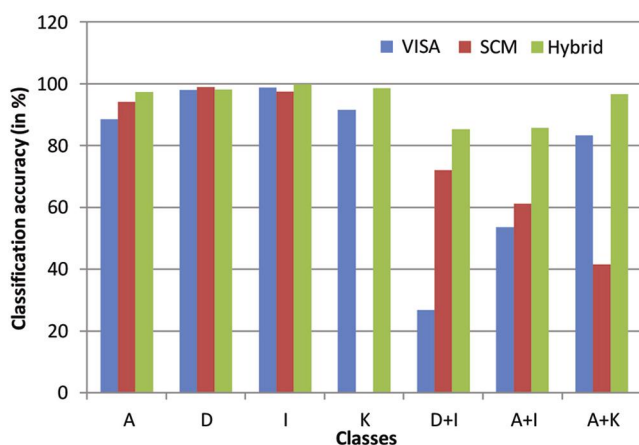
ing spectral channel data. New methods like variable interval spectral average and its combination with spectral feature fitting method find potential for improved mixed pixel classification performance. The images from Ch-1 HySI sensor are shown to be useful in identifying the lunar secondary craters, and help in the relative age estimation of planetary surfaces. The preliminary HySI analysis reveals that the interior wall of the crater is optically more immature compared to the surface of the ejecta deposit of the crater, implying that the gullies and landslides are youthful geomorphic features. The analysis of spectral profiles from HySI indicates that the spectral properties of landslides in the interior walls of the impact crater and the crater ejecta blanket of the host crater are spectrally distinguishable. The above study supports that the HySI spectra with new spectral matching techniques are useful tool for the identification of craters with gully and landslide morphology.

1. Swayze, G. A., Clark, R. N., Goetz, A. F. H., Chrien, T. G. and Gorelick, N. S., Effects of spectrometer band pass, sampling, and signal to noise ratio on spectrometer identification using the Tetracoder algorithm. *J. Geophys. Res.*, 2003, **108**, 9–30; doi: 10.1029/2002JE001975.

2. Schlaper, D., Boerner, A. and Schaepman, M., The potential of spectral resampling techniques for the simulation of APEX imagery based on AVIRIS data; ftp://ftp.geo.unizh.ch/pub/rsl2/paper/1999/AV_WS_99_resamp.pdf

3. Kumar, A. S., Radhika, T., Keerthi, V., Jain, D. S., Dadhwal, V. K. and Kiran Kumar, A. S., Spectral deconvolution and nonoverlap bands sampling for IMS-1 hyperspectral imager data. *J. Indian Soc. Remote Sensing*, 2014, **42**, 429–434.

4. Clark, R. N., Gallagher, A. J. and Swayze, G. A., Material absorption band depth mapping of imaging spectrometer data using a complete band shape least-squares fit with library reference spectra. In Proceedings of the Second Airborne Visible/Infrared Imaging Spectrometer (AVIRIS) Workshop, JPL Publication, 90-54, 1990, pp. 176–186.

5. Jiang, X., Tang, L., Wang, C. and Wang, C., Spectral characteristics and feature selection of hyperspectral remote sensing data. *Inter. J. Remote Sensing*, 2004, **25**, 51–59.

6. Noyel, G., Angulo, J. and Jeulin, D., Morphological segmentation of hyperspectral images. *Image Anal. Stereol.*, 2007, **26**, 101–109.

7. Landgrebe, D., Hyperspectral image analysis as a high-dimensional signal processing problem. *IEEE Signal Proc. Mag.*, 2002.

8. Shaw, G. and Manolakis, D., Signal processing for hyperspectral image exploitation. *IEEE Signal Process. Mag.*, 2002, **19**, 12–16.

9. Guo, B., Gun, S. R., Damper, R. I. and Nelson, J. D. B., Customizing kernel function for SVM-based hyperspectral image classification. *IEEE Trans. Image Proc.*, 2008, **17**, 622–629.

10. Wang, L., Jia, X. and Zhang, Y., A novel geometry based feature selection technique for hyperspectral imagery. *IEEE Geosci. Remote Sensing Lett.*, 2007, **4**, 171–175.

11. Jia, X. and Richards, J. A., Segmented principal components transformation for efficient hyperspectral remote sensing image display and classification. *IEEE Trans. Geosci. Remote Sensing*, 1999, **37**, 538–542.

12. Varshney, P. K. and Arora, M. K., *Advanced Image Processing Techniques for Remote Sensing Hyperspectral Data*, Springer Verlag, New York, 2004.

13. Van der Meer, F., De Jong, S. M. and Bakker, W., Imaging spectrometry: basic analytical techniques. In *Imaging Spectrometry: Basic Principles and Prospective Applications* (eds Vander Meer, F. and De Jong, S. M.), Kluwer Academic Publishers, The Netherlands, 2003.

14. Kumar, A. S., Jayabharathi, S., Manjunath, A. S. and Rao, K. M. M., Fast searching of spectral library database using variable interval spectral average method. *Proc. SPIE*, 2006, **6405**, 64051k-1–6.

15. Van der Meer, F., The effectiveness of spectral similarity measures for the analysis of hyperspectral imagery. *Intern. J. Appl. Earth Obs. Geoinf.*, 2006, **8**, 3–17.

16. Kumar, A. S., Keerthi, V., Manjunath, A. S., Vanderwerff, H. and Van der Meer, F., Hyperspectral image classification by a variable interval spectral average method and spectral curve matching combined algorithm. *Int. J. Appl. Earth Observ. Geoinform.*, 2010, **12**(4), 261–269.

17. Kumar, P. S., Kumar, A. S., Keerthi, V., Goswami, J. N., Krishna, B. G. and Kiran Kumar, A. S., Chandrayaan-1 observation of distant secondary craters of Copernicus exhibiting central mound morphology: evidence for low-velocity clustered impacts on the Moon. *Planet. Space Sci.*, 2011, **59**, 870–879.

18. Kumar, A. S., Kiran Kumar, A. S., Goswami, J. N., Pieters, C. M., Krishna, B. G. and Chauhan, P., Lunar oriental basin: topology and morphology of impact melt region. In 40th Lunar Planetary Science Conference, 2009, 1505.

19. Melosh, H. J., *Impact Cratering: A Geologic Process*, Oxford University Press, New York, 1987.

20. McEwen, A. S. and Bierhaus, E. B., The importance of secondary cratering to age constraints on planetary surfaces. *Annu. Rev. Earth Planet. Sci.*, 2006, **34**, 535–567.

21. Senft, L. E. and Stewart, S. T., Modeling impact cratering in layered surfaces. *J. Geophys. Res.*, 2007, **112**, E11002; doi: 10.1029/2007JE002894.

22. Schultz, P. H. and Singer, J., A comparison of secondary craters on the Moon, Mercury, and Mars. In Proceedings of the Lunar Planetary Science Conference, 1980, pp. 2243–2259.

23. Bart, G. D., Comparison of small lunar landslides and Martian gullies. *Icarus*, 2007, **187**, 417–421.

24. Kumar, P. S. *et al.*, Gullies and landslides on the moon: evidence for dry granular flows. *J. Geophys. Res. Planets*, 2013, **118**(2), 206–223.

25. Chowdhury, A. R. and Murali, K. R., Compact hyperspectral imager with selectable bands in multispectral, hyperspectral and ultraspectral remote sensing technology, techniques and applications. *Proc. SPIE*, 2006, **6405**, 64050U.

26. Kumar, Kiran A. S. *et al.*, Hyper spectral imager for lunar mineral mapping in visible and near infrared band. *Curr. Sci.*, 2009, **96**, 496–499.

27. Mallat, S., A theory of multiresolution signal decomposition: the wavelet representation. *IEEE Trans Pattern Anal. Mach. Intell.*, 1989, **2**, 674–693.

28. Pieters, C., The Moon as a spectral calibration standard enabled by lunar samples: the Clementine example. In Workshop on the New Views of the Moon II, Flagstaff, Arizona, Abstr. 8025, 22–24 September 1999.

29. Fischer, E. M. and Pieters, C. M., Remote determination of exposure degree and iron concentration of lunar soils using VIS–NIR spectroscopic methods. *Icarus*, 1994, **111**, 475–488; doi: 10.1006/icar.1994.1158.

30. Lucey, P. G., Blewett, D. T., Taylor, G. J. and Hawke, B. R., Imaging of lunar surface maturity. *J. Geophys. Res.*, 2000, **105**, 20377–20386.